
Article:
Ikonic, Z, Chen, Z, Indjin, D et al. (1 more author) (2021) Design considerations of intra-step SiGeSn/GeSn quantum well electroabsorption modulators. Journal of Applied Physics. ISSN 0021-8979

https://doi.org/10.1063/5.0067803

PLEASE CITE THIS ARTICLE AS DOI: 10.1063/5.0067803

Journal of Applied Physics

AIP Publishing

Design Considerations of Intra-Step SiGeSn/GeSn Quantum Well Electroabsorption Modulators

Zhichao Chen, Zoran Ikonic, Dragan Indjin, Robert W. Kelsall

School of Electronic and Electrical Engineering, University of Leeds, LS2 9JT, Leeds, UK
chenzhichao1994@hotmail.com
Z.Ikonic@leeds.ac.uk
D.Indjin@leeds.ac.uk
R.W.Kelsall@leeds.ac.uk

Abstract: Theoretical investigation of electro-absorption modulators in the mid-infrared range (>~2μm) is performed, using asymmetric intra-step quantum wells based on $Ge_{1-\eta1}Sn_{\eta1}$/ $Ge_{1-\eta2}Sn_{\eta2}$ heterostructures, with SiGeSn outer barriers. After exploring the parameter space of the Sn content difference, and width ratio of the intra-layers, a linear and much larger Stark shift is realized, compared to that of a square quantum well, without an increase of the total structure width. A modulator based on optimized intra-step quantum well structure with a total well width of 12nm is theoretically predicted to have both a larger peak shift per unit applied field and a larger absorption change than a 12 nm square quantum well device. By analyzing the device performance based on the two figures of merit: (1) Absorption change per applied field and (2) absorption change per applied field squared, and taking 10dB extinction ratio a 44% higher bandwidth per volt and 46% lower power consumption per bit are achieved in intra-step than in a square well. Although the swing voltage for a square quantum well can be reduced by using a larger on-set applied field, and performance could be improved, we found that the intra-step quantum well using zero on-set still retains its advantages when compared to the square quantum well which uses a 0.5V on-set voltage.

Keywords: SiGeSn/GeSn, electroabsorption modulator, **k.p** method, intra-step quantum well

I. Introduction

Silicon-based electronic-photonic integrated circuits (EPICs) are developing fast. Light sources based on Si, Ge, Sn and their alloys have been demonstrated in the past few years [1][2][3]. Different from the standard telecommunication optical wavelength range (1310nm-1550nm), where optical fibers have low transmission loss and signal distortion, the GeSn lasers emit longer wavelengths, typically over 2μm (the first electrically pumped GeSn laser had a wavelength of 2300nm at 100K [3], and a SiGeSn/GeSn multi-quantum-well (MQW) optically pumped laser operated around 2500nm at 90K [4]). Early research on silicon-based electoabsorption modulators, both theoretical (e.g. [5][6][7][8]) and experimental (e.g. [9][10][11]), was focused on the 1310nm-1550nm wavelength range, and mostly used Ge as the optically active material. However, GeSn has recently attracted considerable attention as a material for modulators, in order to expand the wavelength range into the mid-infrared (MIR), both for modulators and other on-chip devices [12][13][14][15].

QWs based on Group-IV materials were shown to offer high speed modulation and low power consumption [16]. Attempts to optimize the performance of the Group-IV QW modulators have been conducted from several aspects. For example, J. Gao, et al.[8] used an 18.5nm wide QW to achieve a low driving voltage, because wider QWs have a stronger quantum-confined Stark Effect (QCSE). However, a poor absorption change or extinction ratio should be expected for wider QWs, because of larger separation of electron and hole wavefunctions when electric field is applied. T. Fujisawa, et al. [17] found that a strain-compensated structure will enhance the absorption under an applied electric field because of stronger carrier confinement in such structures, but they also argued that large carrier confinement will affect the high-speed characteristics. So, for conventional square (symmetric) QWs, there are tradeoffs between the extinction ratio, power consumption and modulation speed.

Another design direction, that was not frequently used in Group-IV structures (in contrast to the conventional structures based on III-V materials such as AlGaAs/GaAs or InP/InGaAsP) is to use QW profiles other than the simple square QWs. An intra-step QW may have a faster absorption peak shift than a square QW [18][19], or may delay the onset of the Stark effect redshift to higher electric fields, followed by a larger change of absorption [20][21]. In this work we focus on the former, aiming to obtain a larger absorption peak shift, which would enable on-chip devices with CMOS compatibility and low driving bias. It has been observed that the advantages of a stepped quantum well structure can be accompanied by a reduced extinction ratio [22], indicating that careful optimization is required to obtain practical device

improvements. In this paper, we systematically investigate the performance of the SiGeSn/$Ge_{1-\eta 1}Sn_{\eta 1}$/$Ge_{1-\eta 2}Sn_{\eta 2}$/SiGeSn intra-step QW in terms of typical figures of merit: the quantum confined stark shift ΔE_{QCSE}, the absorption intensity change -$\Delta\alpha$, $\Delta\alpha/F$ and $\Delta\alpha/F^2$.

The alloy compositions and strain of the QW structures are chosen so that the modulators can work in the MIR region. Therefore, the parameter space for the Sn content is limited to around ~6%-12% for the well layers, the Si composition in the barrier is ~10% to maintain a good carrier confinement and the strain is balanced by a relaxed buffer layer so that the compressive strain in the well and tensile strain in the barrier will be below ~1%.

The Sn compositions of the left and right step are η_1 and η_2. To form an intra-step, we let $\eta_1 \leq \eta_2$, then the left layer will have higher potential for the conduction band and lower potential for the valence band. Another variable parameter is the width ratio of the two layers $R_w = w_1/w_2$ (w_1-left, w_2-right), and we assume the total geometry length ($w_1 + w_2$) to be the same as for the square QW (e.g. 120Å). Then, by searching through the parameter space, we found an optimal choice that has the maximum figure of merit -$\Delta\alpha/F$, and also has good results for other performance criteria. This structure will have a faster peak shift in the range 0-100kV/cm and also slightly improved absorption difference, compared to the square QW with the same width. Thus, a lower power consumption and higher bandwidth can be expected when a minimum requirement for the extinction ratio is fulfilled.

II. Theoretical Modeling

A. *Bandstructure*

We use the 8-band **k.p** method to calculate the band structure and optical properties. This approach offers a good balance between speed and accuracy, showing good agreement with experimental results, e.g. [8], [23]. The single-particle subbands and the wavefunctions in an intra-step QW structure are calculated by solving the total Hamiltonian using matrix finite difference method:

$$\mathbf{H_{8\times 8}} = \mathbf{H(k)} + \mathbf{D(k)} + \mathbf{D_{so}} + q_e F z \tag{1}$$

where $\mathbf{H(k)}$ is the unstrained Hamiltonian, $\mathbf{D(k)}$ is the strain part of the Hamiltonian and $\mathbf{D_{so}}$ is the spin-orbit Hamiltonian, q_e is the electron charge, F the applied field intensity, z the coordinate. The detailed eight-by-eight matrix form of the three parts of the Hamiltonian, the basis functions, and the implementation of FDM are described in detail in [24].

B. *Exciton effects*

The excitonic effects are calculated using the variational method [25]. Although there are other methods which naturally include excitonic effects, such as many-body theory [17] and the Green's function formalism [26], the variational method also gives a good agreement with experiments, after careful calibration, and is easy to be integrated into the 8-band **k.p** framework. Here we only consider the 1s state, because the 2s and 2p states are very weak and can hardly be observed in experiment [27]. The 1s state wave function is denoted as $\phi(\boldsymbol{\rho})$:

$$\phi(\boldsymbol{\rho}) = \sqrt{\frac{2}{\pi}}\frac{1}{\lambda}\exp\left(\frac{-\rho}{\lambda}\right) \tag{2}$$

where ρ is the in-plane separation between electron and hole, and λ is the variational parameter (effective Bohr radius), this can be found by minimizing the exciton binding energy [27]:

$$\begin{aligned} E_{ex}(\lambda) &= \left\langle \phi \middle| -\frac{\hbar^2}{2m_r}\nabla_\rho^2 - V(\rho) \middle| \phi \right\rangle \\ &= \frac{\hbar^2}{2m_r\lambda^2} - \frac{{q_e}^2}{4\pi\varepsilon_s}\int_{-\infty}^{\infty} dz_e \int_{-\infty}^{\infty} dz_h \, |f_n(z_e)|^2 |g_m(z_h)|^2 \left(\frac{2}{\lambda}\right) G\left(\frac{2|z_e - z_h|}{\lambda}\right) \end{aligned} \tag{3}$$

where m_r is the reduced in-plane effective mass, given by $1/m_r = 1/m_e^* + 1/m_{h\|}^*$. The in-plane heavy and light hole effective masses are obtained from Luttinger parameters $1/m_{h\|}^* = (1/m_0)(\gamma_1 \pm \gamma_2)$ ('+' corresponds to heavy holes, and '-' to light holes). The split-off effective mass is given by $1/m_{so}^* = (1/m_0)\{\gamma_1 - E_p\Delta_{so}/[3E_g(E_g + \Delta_{so})]\}$. The values of effective masses used in Eq. (3) are the averages across the whole structure, calculated according to the fraction of wavefunction in each layer. $V(\rho)$ is the interaction potential, ε_s is the permittivity of the semiconductor, z_e and z_h are the coordinate of the electron and hole. f_n and g_m are the n-th and m-th state wavefunctions in the conduction band and valence band. The square of the wavefunction is obtained by summing up the eight components of the normalized

envelope wavefunction at the Brillouin zone centre. $G(x)$ is defined in the Appendix. To simplify the calculation we use a polynomial approximation for $G(x)$ [25]. The detailed expression is shown in the Appendix A. The shape of $E_{ex}(\lambda)$ is shown in Fig.1a. It is a function which has only one minimum and it can be easily found numerically, by searching for zero of its first derivative. Next, in Fig.1b the absolute value of binding energy and Bohr radius dependence on the electric field is shown for the first heavy-hole exciton state. With increasing electric field the absolute value of exciton binding energy decreases and the Bohr radius increases, because the electron and hole wavefunctions move towards opposite sides of the QW, the binding becomes weaker, and the average in-plane extension increases.

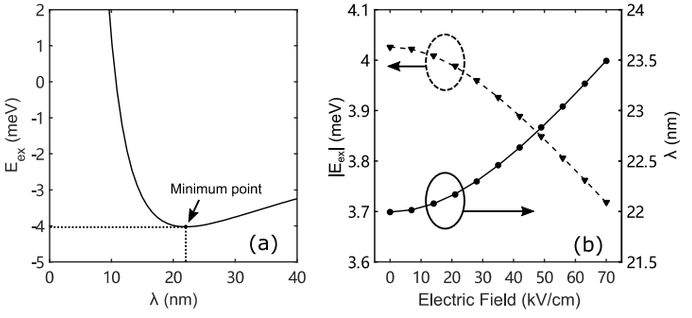

Fig.1. Exciton states in a 10nm $Si_{0.15}Ge_{0.85}$/Ge QW: (a) Exciton binding energy of the first electron and heavy hole state dependence on the variational parameter without electric field; (b) Absolute value of exciton binding energy of first electron-heavy hole state and effective Bohr radius versus the electric field in the range 0-70kV/cm.

C. Optical absorption calculation

The optical absorption has three contributions in our model. The first is the absorption resulting in generation of the 1s exciton state. This can be obtained after solving the exciton problem described in the previous section. By summing up the absorption due to each pair of electron and hole subbands, the contribution of this process is [27]:

$$\alpha_{1s}(\hbar\omega) = \frac{\pi {q_e}^2}{n_r c\epsilon_0 m_0^2 \omega}\frac{1}{L_z}\sum_{n,m}\left(\frac{2}{\pi {\lambda_{nm}}^2}\right)\left|\langle\Psi_{en}^{\mathbf{k}=0}|\mathbf{p_\sigma}|\Psi_{hm}^{\mathbf{k}=0}\rangle\right|^2 \mathcal{V}(\hbar\omega - E_x^{nm}, \Gamma_L, \Gamma_G) \quad (4)$$

where n_r is the refractive index, c is the speed of light, ϵ_0 is the vacuum permittivity, m_0 is the free electron mass, L_z is the length of the period (the sum of well and barrier widths), n and m denote the n-th conduction band and m-th valence band. Note that in the 8-band **k.p** method the spin is already included, so the two degenerate bands with the same energy but opposite spin will have different values of n or m; $\left|\langle\Psi_{en}^{\mathbf{k}=0}|\mathbf{p_\sigma}|\Psi_{hm}^{\mathbf{k}=0}\rangle\right|$ is the momentum matrix element (MME) and the wave functions are taken at the center of the Brillouin zone. $E_x^{nm} = E_{k=0}^{nm} + E_{ex}$ is the exciton transition energy between n-th conduction band and m-th valence band. The broadening in this model is described by the Voigt profile $\mathcal{V}(\hbar\omega - E_x^{nm}, \Gamma_L, \Gamma_G)$ [7]. It includes two types of broadening. One is the homogeneous broadening, depending on the Γ-valley lifetime. A Lorentzian function is usually employed for this type of broadening [7],[28]. The half width at half maximum of the Lorentzian function is denoted as Γ_L. For this lifetime we use the data for Ge because there are not sufficient data for GeSn. We assume that a small amount of Sn will not dramatically influence this parameter. As indicated in [29], the dependence on temperature is rather weak. Here a constant half width at half maximum of Γ_L=3meV is used, corresponding to a carrier lifetime of 110fs [7]. Another component of broadening is inhomogeneous broadening, described by a Gaussian function. The half width at half maximum of the Gaussian function is denoted as Γ_G. This is influenced by the structural fluctuations, and depends on the conditions of epitaxial growth. In general it will also have some dependence on the electric field, which we include by assuming a linear variation of the HWHM Γ_G between 3.32meV and 5meV from 0kV/cm to 160kV/cm [25]. Lastly, to reduce the computation time, the Voigt profile is handled by the method described in [30].

The continuous contribution to absorption, with exciton effects, was calculated from [27]:

$$a_c(\hbar\omega) = \frac{\pi {q_e}^2}{n_r c\epsilon_0 m_0^2 \omega}\frac{1}{L_z}\sum_{n,m}\iint\frac{dk_x dk_y}{(2\pi)^2} S(E)|\langle\Psi_{en}|\mathbf{p_\sigma}|\Psi_{hm}\rangle|^2 \mathcal{V}(\hbar\omega - E_{hm}^{en}(\boldsymbol{k}), \Gamma_L, \Gamma_G) \quad (5)$$

where k_x and k_y are the in-plane wave vectors, and $E_{hm}^{en}(\boldsymbol{k})$ is the transition energy between the conduction and valence subbands in the momentum space, obtained from **k.p** calculation. $S(E)$ is the Coulomb (Sommerfeld) enhancement factor. For a pure 2D exciton, this factor is:

$$S(E) = \frac{s_0}{1 + \exp\left(-2\pi/\sqrt{E_t(\mathbf{k})/R_y}\right)} \tag{6}$$

where $E_t(\mathbf{k}) = (\hbar k)^2/(2m_r)$, and R_y is the exciton Rydberg energy. For a pure 2D exciton $s_0 = 2$. This is a function which is equal to 2 at the band-edge and approaches to 1 when energy tends to infinity. However, it would be inappropriate to use this formula here, because a quantum well has an effective dimensionality between 2D and 3D. It has been previously argued in [26] that the pure 2D enhancement factor will overestimate the continuous spectrum by about 50% in a 10nm GaAs QW. We assume that this overestimation is similar in our case and take $S(E) = 1.33$ as a constant. In Fig.2, the dashed line is the experimentally measured absorption spectrum of a 10nm $Si_{0.15}Ge_{0.85}$/Ge MQW for 0V applied voltage [9]. For the same structure, we found that using 1.33 as the enhancement factor provides better agreement with the experimental results than would be the case with the pure 2D expression. If Eq. (6) is used, the continuous part is too large and the first exciton peak cannot be clearly resolved even at 0V bias.

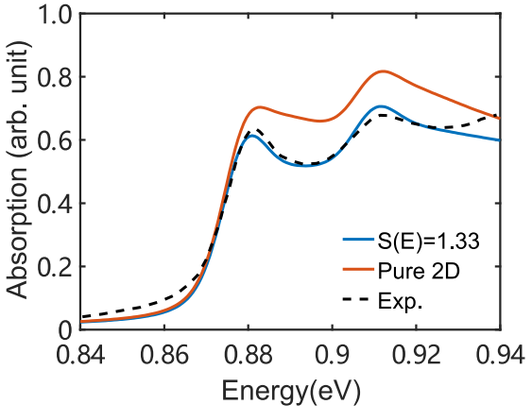

Fig.2. Comparison of absorption spectra when using Eq.(6) (red) and 1.33 (blue) as the Coulomb enhancement factor with the experimental result for a 10nm Ge QW at 0V [9].

The indirect absorption is calculated using a Ge bulk model, as in [31],[32]:

$$\alpha_{ind}(\hbar\omega) = A_{obs}\left[\frac{1}{1-\exp\left(-\frac{E_{ph}}{k_bT}\right)}\left(\frac{\hbar\omega - E_g^L - E_{ph}}{\hbar\omega}\right)^2 + \frac{1}{1-\exp\left(\frac{E_{ph}}{k_bT}\right)}\left(\frac{\hbar\omega - E_g^L + E_{ph}}{\hbar\omega}\right)^2\right] \tag{7}$$

where A_{obs} is a temperature-independent constant. A_{obs} value is taken as 1150cm^{-1}, because the indirect absorption of Ge calculated by Eq.(7) then best fits the experimental results [32]; k_b is the Boltzmann constant; T is the temperature in K; $E_{ph} = 27.8$meV is the optical phonon energy in Ge; E_g^L is the bandgap towards the L-valley. The bulk model will give smaller indirect absorption compared to a QW, but since the incorporation of Sn in the alloy will bring its band-structure closer to that of a direct-gap semiconductor, thus reducing the indirect absorption, this approximation is acceptable. This component will add some insertion loss for photon energies lower than the band gap. The total absorption spectra is calculated by summing α_{1s}, α_c and α_{ind}.

D. Parameters

The parameters of Si, Ge, Sn and their alloys used in 8-band **k.p** and absorption modelling can be calculated from Vegard's law:

$$G_{SiGeSn} = \eta_{Si}G_{Si} + \eta_{Ge}G_{Ge} + \eta_{Sn}G_{Sn} - \eta_{Si}\eta_{Ge}B_{SiGe} - \eta_{Si}\eta_{Sn}B_{SiSn} - \eta_{Ge}\eta_{Sn}B_{GeSn} \tag{8}$$

where G is the parameter of a pure element, η represents the concentration of that element, B is the bowing parameter for the binary alloy. The parameters used in Eq. (8) are given in Table I. Note that for the parameters which do not have bowing parameters we have used linear interpolation. The bowing parameters of SiSn are not shown because these data are not available. Although some research has indicated the existence of bowing of the Γ-bandgap and L-bandgap [41],[42], the Si and Sn contents are rather small compared to Ge content, so the overall difference caused by this bowing in SiGeSn will be much smaller than it would be in binary SiSn. Additionally, some other parameters were not calculated

using Eq.(8), because the experiments and calculations were not conducted across the full parameter space of compositions, i.e. the Sn content is limited below ~15% in these cases, and the results may not be so accurate when Sn content exceeds this value. These parameters are then given by fitted quadratic interpolation. As shown in Table II, to calculate some parameter of the ternary $Si_xGe_{1-x-y}Sn_y$, we first considered the GeSn part separately, and calculated its value by using interpolation with bowing. Si and GeSn were then linearly combined to obtain the final parameter value for the specific ternary alloy composition. It should also be noted that here we introduced the bowing of Luttinger parameters of SiGe using the method described [24].

Table I. The parameters of Si, Ge, Sn and bowing parameters for SiGe and GeSn

Parameter	Si	Ge	Sn	B_{SiGe}	B_{GeSn}
Lattice constant, a_{lat}(Å)	5.4307[a]	5.6579[a]	6.489[a]	0.026[a]	-0.041[a]
Split-off energy, Δ_{so}(eV)	0.044[a]	0.297[a]	0.8[a]		
Bandgap (Γ-valley), E_g^{Γ}(eV)	4.185[a]	0.8981[b]	-0.38[a]		3.02[c]
Bandgap (L-valley), E_g^{L}(eV)	2.716[a]	0.74[a]	0.1[a]		1.23[c]
Bandgap (Γ_{25}-Γ_{15}), E_g'(eV)	3.4[b]	3.124[b]	/		
MME (Γ_{25}-Γ_{15}), E_P'(eV)	14.4[b]	17.5[b]	/		
Valence band offset, E_v(eV)	-1.17[d]	-0.69[d]	0[d]		
Deformation Potential (CB), a_c(eV)	-10.06[a]	-8.24[a]	-6[a]		
Deformation Potential (VB), a_v(eV	2.46[a]	1.24[a]	1.58[a]		
Deformation Potential, b(eV)	-2.1[a]	-2.9[a]	-2.7[a]		
Deformation Potential, d(eV)	-5.3[e]	-4.8[e]	-4.1[e]		
Deformation Potential (L), a_L(eV)	-0.66[a]	-1.54[a]	-2.14[a]		
Stiffness constant, C_{11}(GPa)	165.77[a]	128.53[a]	69[a]		
Stiffness constant, C_{12}(GPa)	63.93[a]	48.26[a]	29.3[a]		
Refractive index, n_r(4.1μm)	3.41[f]	3.93[f]	6.18[g]		
Varshni, a_{vshni}^{Γ}(eV/K)	3.91×10^{-4}[a]	5.82×10^{-4}[a]	0[a]		
Varshni, b_{vshni}^{Γ}(K)	125[a]	296[a]	0[a]		
Varshni, a_{vshni}^{L}(eV/K)	4.774×10^{-4}[a]	4.774×10^{-4}[a]	0[a]		
Varshni, b_{vshni}^{L}(K)	235[a]	235[a]	0[a]		
Permittivity, $\epsilon_r(\epsilon_0)$	11.7[h]	16.0[h]	24.0[h]		

[a] [33]; [b] [34]; [c] [35]; [d] [36]; [e] [37]; [f] [38]; [g] [39]; [h] [40]

Table II. Parameters of $Si_xGe_{1-x-y}Sn_y$ calculated by interpolation

Parameter	Si	Interpolation-GeSn, y′=y/(1-x), y′<0.15
Luttinger, γ_1	4.22[a]	$11.11 + 28.53y' + 105.2y'^2$ [b]
Luttinger, γ_2	0.39[a]	$3.252 + 13.95y' + 52.75y'^2$ [b]
Luttinger, γ_3	1.44[a]	$4.689 + 14.37y' + 52.57y'^2$ [b]
MME, E_p(eV)	21.6[a]	$25.61 - 2.319y' + 0.2463y'^2$ [b]
Effective mass (Γ), $m_e^{\Gamma}(m_0)$	0.241[c]	$0.042 - 0.1436y' + 0.1026y'^2$ [b]

[a] [33]; [b] [43]; [c] [34]

III. Results and discussion

A. *Comparison with experimental results*

We have first verified the accuracy of our model and the reliability of the material parameters by comparing our calculation with experimental results from [9]. The calculations were made for the range of parameters as follows: (1) The experimentally measured absorption is given for 0V-4V bias, and the field intensities used in calculations, corresponding to 0-4V bias voltage, were obtained from Fig.4 in [9], so the values are 15.03 kV/cm, 37.33 kV/cm, 58.95 kV/cm, 80.81 kV/cm and 102.45 kV/cm; (2) The $Si_{0.15}Ge_{0.85}$/Ge QW structure was grown on a $Si_{0.1}Ge_{0.9}$ buffer, and it has been previously discussed that the buffer layer is not fully relaxed, and that some tensile strain exists because of the high temperature annealing process [44]. This, however, was not mentioned in [9]. We have assumed that the tensile strain in $Si_{0.1}Ge_{0.9}$ buffer is 0.15% (within the typical range from experiments as indicated in [7]), which gives good agreement

with experimental results. (3) The half width half maximum (HWHM) of the heavy hole exciton peak reported in [9] was ~8meV, so for the purposes of this validation only, Γ_G is not varying with the electric field as discussed previously (just in this case, for comparison purposes). Instead, Γ_G was assigned a constant value of 5meV [7], together with $\Gamma_L = 3$ meV, the HWHM of the calculated exciton peak using Voigt profile is then similar to the experimentally measured result (~8meV).

Fig.3a, shows the calculated absorption spectra compared alongside the experimental data. Fig.3b shows the measured exciton peak shift and calculated values, using the **k.p** method together with the resonant tunneling method [9]. Our work generally shows good agreement with experimental results, especially at low voltages. At 0V the measured experimental exciton peaks for HH1 and LH1 are at ~0.88eV and 0.91eV, respectively. Our calculated results are 0.88eV for HH1 and 0.911eV for LH1. The errors at 0V are 1meV. However for large electric fields, the calculated Stark shift is smaller than the experimental one. In Fig.3b, the peak shift has a difference of ~5meV at 5V (~100kV/cm) using our **k.p** model, which is, nevertheless, closer to the experimental data than the resonant tunneling method (TRM) calculation. The discrepancy may be due to additional non-uniform electric fields, caused by background doping, which have not been included in our model. Secondly, the absorption intensity at the exciton peak is smaller in our calculation. This has been discussed in [23], where the authors also reported such a difference between their results and the experiments, which they suggested is due to an increased probability of indirect absorption, because high electric fields will cause more heating in the structure, generating more phonons which can mediate the indirect process. But overall, the validation indicates that this model is good enough to analyze, predict and compare the modulation performance of square QWs and the intra-step QWs, especially since we are interested in low voltage applications. Additionally, the differences between experiment and theory described are relatively consistent across all cases considered, QW designs will not be inhibited by these effects.

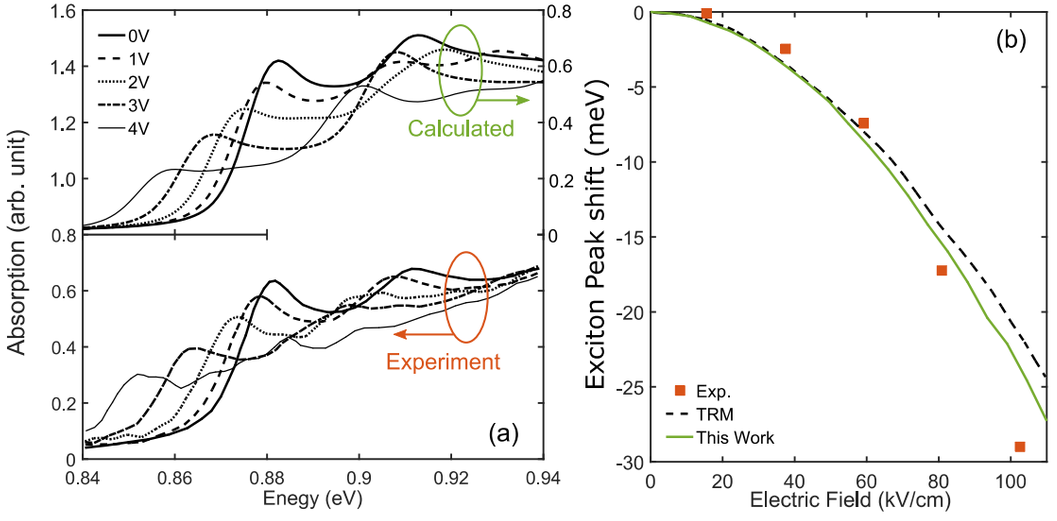

Fig.3. (a) The comparison of calculated and experimental TE absorption spectra at room temperature for 10 nm $Si_{0.15}Ge_{0.85}$/Ge MQW grown on a $Si_{0.1}Ge_{0.9}$ virtual substrate with bias voltages in the range 0V-4V. The top figure is calculated in this work and the bottom figure is the experimental absorption derived from photocurrent spectra [9]; (b) Comparison of C1-HH1 exciton peak shift from measurement [9] (red square), tunneling resonance method [9] (dashed line) and from **k.p** calculations in this work (green solid line).

B. Quantum confined Stark effect in intra-step quantum wells

The QCSE behavior of the intra-step QWs is different from that of square QWs. In order to understand the difference between intra-step QW and square QW, we can qualitatively analyze it by perturbation theory, based on infinite QW. By treating $H' = q_e F z$ as the perturbation, the state energy within the second-order perturbation theory is [27]:

$$E = E_n^{(0)} + H'_{nn} + \sum_{m\neq n} \frac{H'_{nm}}{E_n^{(0)} - E_m^{(0)}}$$
$$= E_n^{(0)} + \left\langle \psi_n^{(0)} \middle| q_e F z \middle| \psi_n^{(0)} \right\rangle + C_n \frac{\left(\pi q_e F L_{eff}\right)^2}{2E_1^{(0)}} \quad (9)$$
$$= E_n^{(0)} + \langle \hat{z} \rangle q_e F + C_n \frac{\left(\pi q_e F L_{eff}\right)^2}{2E_1^{(0)}}$$

in which the superscript '(0)' represents the unperturbed solution (i.e. the wavefunction and energy when F=0kV/cm), n is the the subband index., $\langle \hat{z} \rangle$ is the average coordinate of the wavefunction, and L_{eff} is the effective well width. C_n is the coefficient of the n-th subband. For the first subband $C_1 \approx -2.19 \times 10^{-3}$. Next, the transition energy between the first conduction and valence subband, with the applied field F, is then:

$$E_{h1}^{e1}(F) \approx E_{h1}^{e1}(F=0) - \left[(\langle \widehat{z_{h1}} \rangle - \langle \widehat{z_{e1}} \rangle) q_e F + 2.19 \times 10^{-3} \frac{(m_e^* + m_h^*) {q_e}^2 {L_{eff}}^4}{\hbar^2} F^2 \right] \quad (10)$$

For the convenience of explanation, the Stark shift within the square bracket is further simplified by a quadratic function of the electric field F:

$$\Delta E_{QCSE} \approx (\langle \widehat{z_{h1}} \rangle - \langle \widehat{z_{e1}} \rangle) q_e F + 2.19 \times 10^{-3} \frac{(m_e^* + m_h^*) {q_e}^2 {L_{eff}}^4}{\hbar^2} F^2 \quad (11)$$
$$= S_1 (q_e F) + S_2 (q_e F)^2$$

where S_1 and S_2 are the coefficients of the first and second order of the product of electric field F and electron charge q_e. S_1 is simply the difference between the average coordinates of the electron and hole wavefunctions. The unperturbed wavefunctions of the intra-step QW and square QW are shown in Fig.4. For a square QW (Fig.4b) the average coordinates of both electron and hole wavefunctions located at the center of the QW, so $S_1 = 0$, and the Stark shift depends only on S_2 which is proportional to ${L_{eff}}^4$. The coefficient S_2 also contains the sum of the effective masses $(m_e^* + m_h^*)$, and higher Sn content material has smaller effective masses, but the Sn content in the well layer varies within a very limited range, and the Stark shift is therefore less sensitive to the effective mass than to the well width L_{eff}. Fig.5 shows the Stark shift of 10-14nm square QWs with Sn content of 8.25% - 10.25% in the well. As can be seen, 2% change of the Sn content doesn't have much influence on the Stark shift, but a significant difference can be seen when varying the well width from 12 to 14nm. Therefore, to obtain a larger Stark shift in square wells, a larger well width is usually used, but at the same time a smaller absorption change is expected, because carriers are easier to separate to the opposite sides in a wider QW.

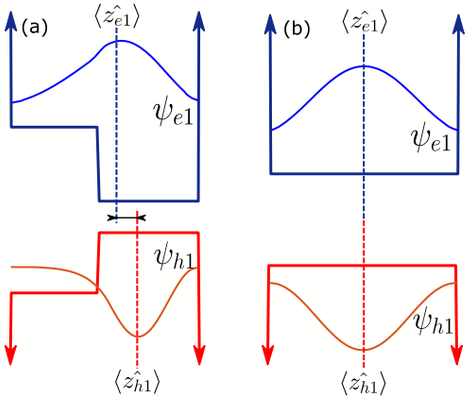

Fig.4. The first conduction band and valence band envelope wavefunctions (offset by energy levels) of (a) infinite intra-step QW; (b) infinite square QW.

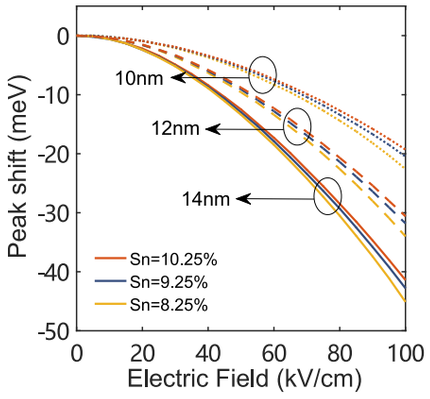

Fig.5. Stark shift versus electric field in square QW with different well widths and Sn contents in the well. The influence of effective mass to the QCSE is much smaller than that of well width.

Since holes have a larger effective mass than electrons, the first hole subband in an intra-step QW has the wave function more confined in the deeper intra-well, while the first electron subband may be above the deeper well, and thus have a less confined wavefunction. Therefore, S_1 is usually not zero for the intra-step QW, consequently, the Stark shift will be more linear compared to the square QW case. Although there is no analytical expression for S_1, it can be engineered by adjusting the ratio of widths of the shallower and deeper well layers w_1/w_2, and by changing the depth of the deeper intra-well by controlling the alloy composition of the two intra-layers.

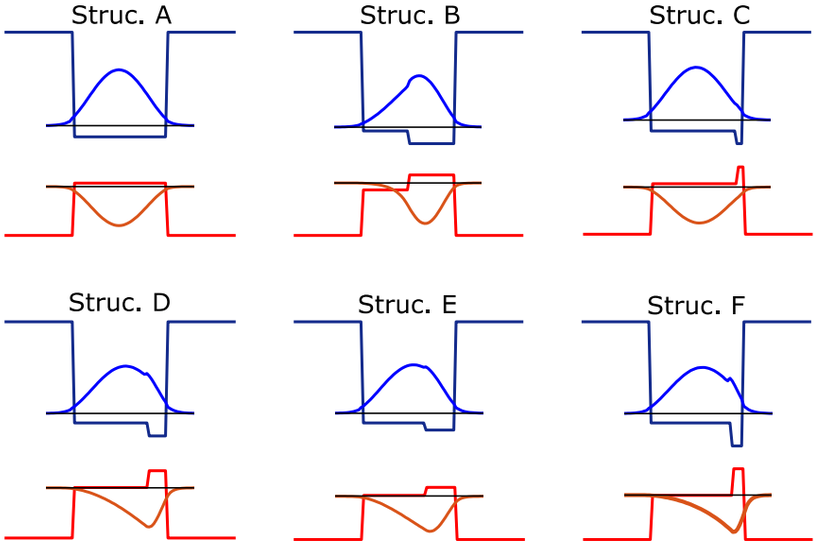

Fig.6. Conduction band and heavy hole band potential profiles and subband energies of structures A-F, Note that the HH1 of structure D, E and F is located just at the edge of the intra-QW.

Table III. Well widths and Sn contents of the intra-layers of structures C, E, A and B

	w_1	w_2	η_1^{Sn}	η_2^{Sn}
structure A	14 nm	/	9%	/
structure B	7 nm	7 nm	8%	10.2%
structure C	13 nm	1 nm	8%	10.2 %
structure D	11 nm	3 nm	8%	10.2%
structure E	9.5 nm	4.5 nm	8%	9.2 %
structure F	12 nm	2 nm	8%	12%

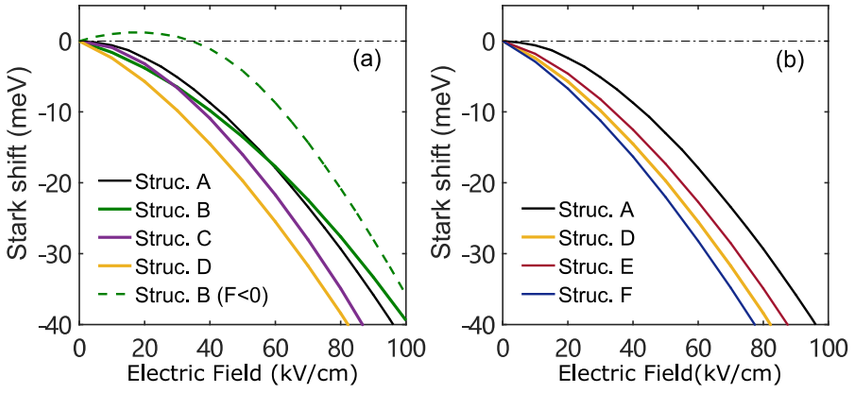

Fig.7. Comparison of quantum confined stark shift versus the electric field between (a) structures A, B, C and D; (b) structures A, D, E and F.

In this section, without considering any optical performance feature, we only focus on the QCSE. Six typical structures are used as examples to illustrate how a larger Stark shift (within the range of 0-100 kV/cm) can be achieved by intra-step QW without changing the total geometry width. All the structures, with the total width of 14nm, use $Si_{0.1}Ge_{0.835}Sn_{0.065}$ as barriers, and $Si_{0.1}Ge_{0.82}Sn_{0.08}$ as the substrate. The potential profiles and energy levels of these structures are shown in Fig.6 and the corresponding values of well widths and Sn content in the two intra layers are shown in Table III. The Stark shift versus the applied field dependence for these structures are compared in Fig.7.

An intra-step QW does not guarantee a larger Stark shift than a square QW. Comparing structure A and B, as is shown in Fig.7a, structure B has a larger Stark shift than structure A from 0kV/cm to 60kV/cm, but this becomes smaller beyond 60kV/cm. Although the asymmetric intra-step QW has a none-zero first-order perturbation term, the Stark shift is also determined by the coefficient S_2. Note that the coefficient S_2 in Eq. (11) is derived for an infinite square QW. According to the calculations, the fitted S_2 is usually smaller for an intra-step QW than for a square QW of the same size when $F > 0$. We didn't derive the exact expression for S_2 for an intra-step QW, but this is likely to correspond to taking a smaller effective width L_{eff} in Eq.(11). So, for an intra-step QW, if the first-order coefficient S_1 is not large enough, we can only see a larger Stark shift for low applied fields, but for larger fields it will be smaller than for the square QW.

For some Sn contents in the two intra-layers the largest Stark shift (for the applied field below 100kV/cm) can be found by adjusting the width ratio only. With the same Sn contents in the two intra-layers, as in structure B, by increasing the width ratio the largest QCSE was found when the width ratio reaches $R_w \approx 11/3$. We denote this as structure D, the QCSE curve is plotted as the lowest curve (yellow solid line) in Fig.7a. Keeping the width ratio increasing will reduce the QCSE, because for width ratio larger than (11/3), a narrower intra-QW is formed. Then the HH1 is above the edge of the deeper intra-well, and the structure starts to behave more like a square QW. To show this trend, we use structure C, with its intra-QW 1nm wide. Its wave function (see Fig.6) looks very similar to the wave function of the square QW, the first order coefficient of structure C is only $S_1 = 0.7$nm, compared with 2.4nm for structure D. As can be seen in Fig.7a, Stark shift of structure C is reduced because of a smaller first order perturbation term.

Although structure D has the highest QCSE for the fixed Sn content combination of 8% and 10.2%, it is still not the largest if we allow the Sn content to be varied. So, by using different Sn content in the intra-QW we next tested the

structures with deeper and shallower intra-layer than in structure D, the corresponding width ratio with the largest Stark shift can be found by repeating the procedure of finding structure D. The width ratio for the largest Stark shift with a particular Sn contents combination is denoted as R'_w. Structure E and F are the examples shown here, with a shallower and deeper intra-QW respectively. From Table III and Fig.6, we can see that for deeper intra-well (structure F) R'_w was found to be larger. In contrast, shallower intra-well (structure E) will have a smaller R'_w. By comparing the Stark shift of structure D, E and F in Fig.7b, the narrower and deeper intra-well have a larger Stark shift. From this trend, we can deduce that if the constraints on the parameters are relaxed, an even larger Stark shift can be obtained by forming an even narrower and deeper intra-well. However, it is easy to see that such improvement is limited by the total structure width. As the first-order perturbation term $S_1 = \langle \widehat{z_{h1}} \rangle - \langle \widehat{z_{e1}} \rangle$ cannot exceed $(w_1 + w_2)/2$, we expect that a very limited improvement can be obtained by using more "extreme" cases. So we do not expect that very narrow and deep intra well would be used in realistic structures, because of the fabrication difficulties coming from growing a thin layer with large alloy content variation. It is worth mentioning that, by looking at the subband and potential profiles in Fig.6, an interesting pattern for both D, E and F can be observed, that their HH1 states are located just at the edge of the intra-QW. For some other combinations of Sn content, this pattern also exists. Although we currently do not have theoretical explanation for this, it could be a potential criteria pointing when the largest Stark shift for some combination of Sn contents is achieved.

The Stark shift behavior of the square QW is independent of the electric field direction. However this is not the case for intra-step QW. This phenomenon is also simulated using our model. For the case shown in Fig.4a, $\langle \widehat{z_{h1}} \rangle - \langle \widehat{z_{e1}} \rangle$ has a positive value. So, if a forward bias is applied (i.e. $F > 0$), S_1 and S_2 will have the same sign, and a larger Stark shift near $F = 0$ can be expected. If $F < 0$, then S_1 and S_2 will have opposite sign, and in this case the transition energy will initially have a blue shift, but this will convert to red shift at some point, as can be seen from the green dashed line (structure B, F<0) in Fig.7a, the red shift starts at ~38kV/cm. This particular feature of delaying the red shift allows a higher onset voltage, and this has been used for high-optical power modulation [20],[21]. However, this is not the topic of this work, it will not be further discussed here.

C. *Figures of merit and device performance*

In this section we compare and discuss the general performance of the square QW and step QW, in terms of various figures of merit – the exciton peak shift ΔE_x, absorption intensity change $\Delta\alpha$, $\Delta\alpha/F$, and $\Delta\alpha/\Delta F^2$[27],[45],[46]. Here we set the total structure width as 12nm. As a control variable, the sum of the Sn contents in two intra-layers is 18% (i.e. $\eta_1^{Sn} + \eta_2^{Sn} = 18\%$). The buffer layer is $Si_{0.1}Ge_{0.82}Sn_{0.08}$, and is assumed to be fully relaxed. The barrier width is taken as 10nm $Si_{0.1}Ge_{0.835}Sn_{0.065}$. In this case the barrier will have 2.28% tensile strain and the GeSn well region will have a compressive strain (6% for $Ge_{0.91}Sn_{0.09}$). By searching the parameter space for the well width ratio w_1/w_2 and the difference between Sn compositions of the two intra-layers $\Delta\eta_{Sn} = \eta_2^{Sn} - \eta_1^{Sn}$, we find structures which have better performance, in terms of all four above mentioned figures of merit, compared to the square QW with 9% Sn in the well. Note that we set the boundaries of the Sn content in the well layer as 6%~12%, in order to keep the operating region within the MIR band, and to maintain good carrier confinement for the given barrier height.

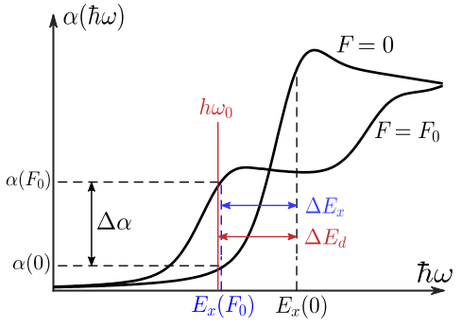

Fig.8. The absorption coefficient of a GeSn quantum well modulator at two different biases: 0 and F_0.

For different intra-step structures the transition energy e1-hh1 for zero bias field is different, and to test different structures we compared the change of absorption at the exciton transition energy when the same peak shift, $\Delta E_x = E_x(0) - E_x(F_0)$, is achieved by applying appropriate bias F_0. (Note that the definition of the exciton peak shift ΔE_x is

slightly different from the Stark shift ΔE_{QCSE} mentioned in the previous section, but since the change of exciton binding energy E_{ex} is only ~1meV for fields in the range 0-100kV/cm, and it is much smaller than the change of the transition energy, we can take $\Delta E_{QCSE} = \Delta E_x$). Although the absorption peak is not located exactly at the calculated exciton transition energy E_x, the real peak is very close to E_x, and it is proportional to the absorption at E_x. When a reasonably large Stark shift is achieved we can take the detuning energy ΔE_d to be the same as the Stark shift energy (i.e. the operating photon energy $\hbar\omega_0$ is equal to the exciton transition energy E_x when a field of F_0 is applied). Then the absorption intensity change is measured at $E_x(F_0)$ as $\Delta\alpha = \alpha(F_0) - \alpha(0)$. To make this clearer, the parameters mentioned above are denoted in Fig.8.

For convenience, instead of varying $\Delta\eta_{Sn}$ and R_w directly in the code, we vary the Sn content η_2^{Sn} and the width w_2 of the intra-QW with steps of 0.25% and 0.5nm respectively. The Sn content and width of the intra-barrier are then calculated as: $\eta_1^{Sn} = 18\% - \eta_2^{Sn}$ and $w_1 = 12nm - w_2$. The figures of merit of these structures, $\Delta\alpha$, $\Delta\alpha/F$, and $\Delta\alpha/\Delta F^2$, are then plotted versus ΔE_x, and QCSE is plotted against the electric field. Next, following the design principle of maximizing the figure of merit $\Delta\alpha/F$ [45], and to ensure the superiority of the other three figure of merit compared with the square QW at the same time, we checked these plots and found the optimum structure (structure II) which has Sn contents of $\eta_1^{Sn} = 7.25\%$ and $\eta_2^{Sn} = 10.75\%$, and the widths of the intra-layers are $w_1 = 8.5nm$ and $w_2 = 3.5nm$. Although the figure of merit $\Delta\alpha/F$ can be further increased by using a narrower and deeper intra-well, because of a larger Stark shift in such a structures (similar to the method to obtain a larger Stark shift introduced in the previous section), the calculations show that only insignificant improvements can be achieved when using intra-well width less than 3.5nm, because a much smaller change of absorption, compared to the square QW case, is obtained if the intra-well width is less than ~3nm, and the improvement of the Stark shift is not so obvious in these thin-layer structures. Moreover, a larger change of the alloy composition in the two intra layers will increase the difficulty of growing such a structure. Hence, the structure II seems to be a more practical example, to be discussed further, than other extremely thin-layer cases. For convenience, to compare realistic performance of an intra-step QW and square QW at the same operating energy, we adjust the Sn content in the Square QW from 9% to 8.5% for the example shown here, so that this 12nm square QW (structure I) has the same transition energy at zero field as does the structure II. In the previous section we have shown how a larger Stark shift is realized by adjusting the parameter of the intra-step QW. But a larger QCSE does not necessarily have the best performance regarding different figures of merit. To investigate this argument, another intra-step QW (structure III), which has a larger QCSE than structure II, is also presented. This has the same Sn content in the two intra-layers as structure II ($\eta_1^{Sn} = 7.25\%$, $\eta_2^{Sn} = 10.75\%$), but has a narrower intra-well (2nm). The TE absorption spectra for applied field in the range 0-100kV/cm are shown in Fig.9a,b,c. The TM absorption is not shown here because LH state is much higher in this case, and HH state does not contribute to the TM polarization absorption. Although structure III has a different transition energy at zero field from the other two, in order to compare them we can still assume their on-set exciton peak as the original point and plot the figures against the peak shift energy in one graph. Again, this is just for the convenience of comparison. To design a structure with similar performance and different transition energy, we can refer to the alloy composition difference and width ratio of the original structure, then shift the Sn content to achieve the required transition energy, because the geometry inside the well is the major aspect that affects the optical behavior of the structure, so it will remain the same if the shift of the Sn content is not very large. Fig.9d compares the absorptions at the exciton peak against the peak shift energy for electric field in the range 0-100kV/cm. The three curves in Fig.9d are very close to each other, but there are still some details that can be discussed. First, for both intra-step QWs the absorption at low electric field is smaller than for the square QW because the asymmetric structure reduces the overlap of the wavefunctions. But for structure II the absorption at exciton energy decreases more slowly against the exciton peak shift, compared to structure I. So, after a 10meV shift the structure II has a larger absorption peak. Secondly, the absorption edge of square QW doesn't have a significant shift when small field is applied. However, for the step QWs the edges are changing more rapidly and more uniformly with increasing electric field. As explained previously, this is because the step QW will have a more linear Stark shift behavior, because asymmetric structures include the first-order perturbation term.

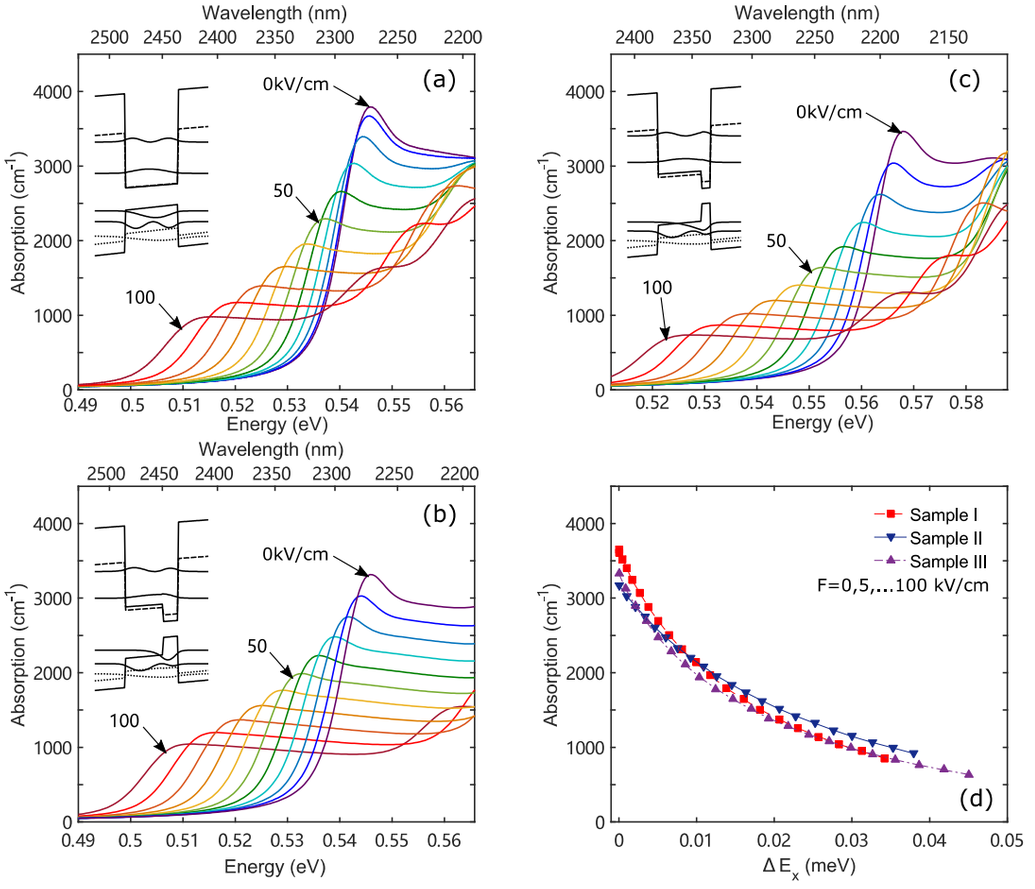

Fig.9. Comparison of the TE absorption spectra (T=300K) for (a) structure I, (b) structure II, (c) structure III. Schematic QW band diagrams and wavefunctions are shown in the insets. The dashed line and dotted line represent the L-valley and LH respectively. (d) The absorption at exciton peak against the energy shift.

In Fig.10, we compare the four figures of merit of structures I-III. Again, the exciton peak shift is the difference between the exciton transition energy at zero field and for finite field F (0-100kV/cm), and the absorption change is measured at the exciton transition energy existing at any particular F, from the residual absorption at zero field. In Fig.10a, the Stark shift for the intra-step QW is larger than for the square QW, but it's not the largest within the parameter space. Structure III has the largest Stark shift, but the smallest absorption change among these three structures. Structure II, compared to the square QW, maintains a larger absorption change and a larger peak shift at the same time. Hence, for $\Delta\alpha/F$ as the figure of merit, the structure II is much better than structure I and slightly better than structure III in the whole range of peak shifts. Additionally, we also give the data for another similar figure of merit, the absorption change per applied field square - $\Delta\alpha/\Delta F^2$, which was used in [47]. Maximizing $\Delta\alpha/\Delta F^2$ is equivalent to minimizing the drive power per bit when a certain contrast ratio of absorption is reached. The intra-step QWs again have better performance than the square QW, however the situation is different from $\Delta\alpha/F$: structure III is slightly better than II here, because this figure of merit is more sensitive to the change of applied field. We have magnified the tail of the curves in Fig.10d and, as can be seen, the improvement obtained over the square QW is as large as 50%, even for large peak shifts. In Fig.10b, the absorption changes for the three structures reach their peak when the peak shift is around ~11meV. In Fig.10c, the maxima of $\Delta\alpha/\Delta F$ appear around ~8meV, and in Fig.10d, the maxima of $\Delta\alpha/\Delta F^2$ appear at even smaller energy (<5 meV). Although the goal of the design is to maximize this figure of merit, the question of whether the detuning energy can be so small to maximize $\Delta\alpha/\Delta F$ or $\Delta\alpha/\Delta F^2$ is further restricted by the requirement of the extinction ratio (ER) and insertion loss (IL). A very small detuning energy will bring about a large IL and a small ER. Here we take the photon energy as a relative parameter, but for a certain photon energy (operating wavelength), to have a proper detuning one has to change the material composition. The on-set transition energy is ideally away from the operating photon energy.

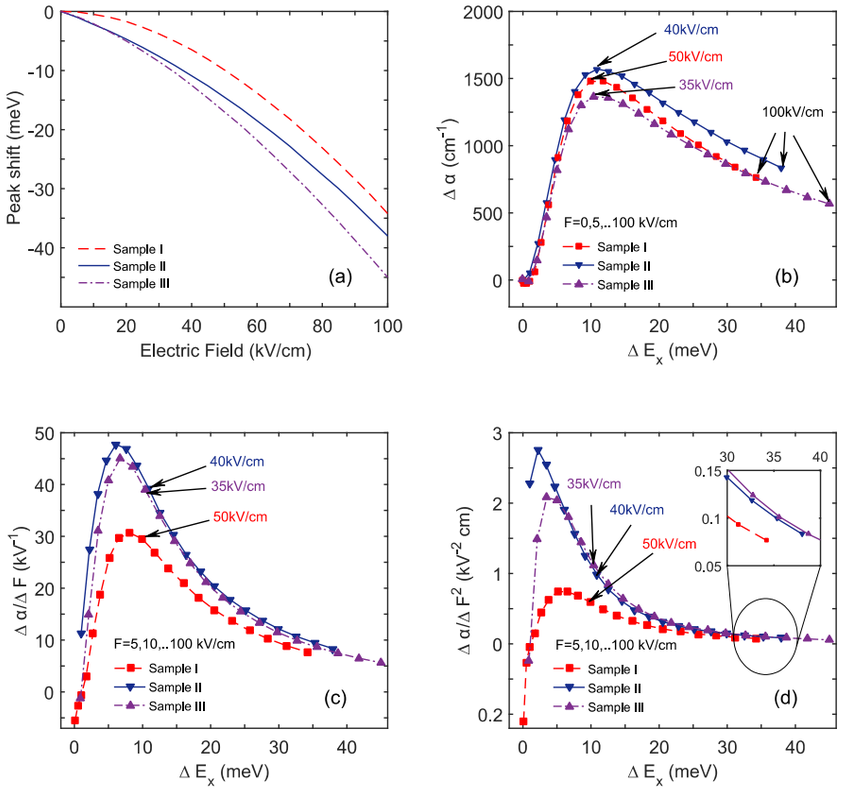

Fig.10. Comparison of the figures of merit: (a) Peak shift against the electric field; (b) Absorption change-$\Delta\alpha$ against the exciton peak shift; (c) $\Delta\alpha/\Delta F$ against exciton peak shift; (d) $\Delta\alpha/\Delta F^2$ against peak shift for electric field in the range 0-100kV.

Note that in Fig.10 we assume the on-set applied field to be 0kV/cm. For a square QW, the peak shift is very small near 0kV/cm, but larger for larger fields. A typical method used to reduce the swing voltage is to set the on-set voltage to some non-zero value. We found that for square QW (structure I), if we choose the on-set applied field for the square QW to be 40kV/cm, it will have the largest figure of merit $\Delta\alpha/F$, and it's even slightly higher than that of the intra-step QW (structure II) with 0kV/cm on-set. Further increasing the on-set from 40kV/cm will not improve this figure of merit, because the peak shift is fairly linear in this range, and smaller absorption is expected for high applied field. For $\Delta\alpha/\Delta F^2$, the improvement from using a larger on-set is more obvious, because this figure of merit is more sensitive to the shift rate and a much higher value can be reached if the on-set applied field is as high as 60kV/cm. Note that the peak shift here is defined as the shift of the exciton energy from its value at the non-zero on-set. These two figures of merit for the square QW (structure I) for 10meV exciton shift with different on-set applied field are shown in Fig.11. As can be seen, the intra-step QW using 0kV/cm on-set keeps its advantage for the $\Delta\alpha/\Delta F$ figure-of-merit almost always, except when the on-set for the square QW is chosen to be ~35-45kV/cm. For the $\Delta\alpha/\Delta F^2$ figure-of-merit, the square QW using an on-set field higher than 20kV/cm can have a better figure of merit compared to the intra-step QW using zero on-set. Similarly, the figures of merit for intra-step QWs can also be improved by choosing a non-zero on-set field, but this is not what we want to achieve here, because in practical applications using a high voltage region for modulation may cause various problems such as current leakage and device breakdown. Since GeSn is still under development as a material for the active region of a modulator, it is presently uncertain what voltage can be tolerated in such structures. For intra-step QWs, because a linear Stark shift exists from the outset, any voltage region, starting from zero bias, can be used for modulation. The on-set voltage can be set to zero without wasting any swing voltage for modulation. This indicates that the intra-step QW is more suitable for low-voltage operation, which is a basic requirement for on-chip devices.

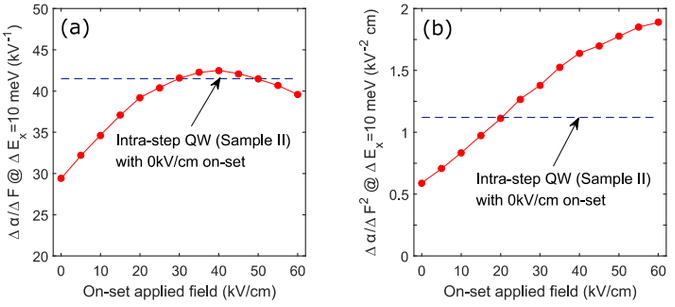

Fig.11. Figures of merit of the square QW at 10meV peak shift when using different on-set applied fields. (a) $\Delta\alpha/\Delta F$ (kV^{-1}) (b) $\Delta\alpha/\Delta F^2$ (kV^{-2}cm). The figures of merit of the intra-step QW (structure II) with 0kV on-set are also shown (dashed blue lines) for comparison.

The proposed optimum intra-step structure (structure II) based on zero on-set voltage does not include any built-in bias, so zero bias voltage implies zero field within the intrinsic region. The above analysis indicates that if a significant built-in bias existed, then a different geometry may be used to optimize the modulator performance. It is reasonable to assume that the performance can always be improved by considering a different potential profile of the QW. This does not necessarily have to be limited to an intra-step QW. In fact, in III-V material systems, attempts to search for broken-symmetry structures in order to achieve a particular functionality have already been made by applying genetic algorithms [48]. This demonstrates that the QW profile engineering can be a promising way to optimize optoelectronic properties for different device requirements.

Finally, we estimate the device performance at a photon energy of 0.53eV (corresponding to a wavelength of ~2340nm) using a typical waveguide design for the modulator. The schematic diagram of such a structure is shown in Fig.12. The 10×multi-quantum well layers with 12nm wells and 10nm barriers have a total thickness of 230nm and are sandwiched between two 50nm intrinsic spacer layers. The total length of the intrinsic region d_i is therefore 330nm. We will not perform a detailed analysis of the length of p-doped buffer layer and n-doped layer, as this will influence the optical confinement factor, which is not calculated here: instead we use the value from [7]. The p-doped buffer layer is 0.5μm and the n-doped layer is 0.1μm thick. The optical confinement factor Γ_c is set to 0.36, which is achieved in [49] using an MQW active layer with a similar thickness (210nm). The width of the waveguide-w_g is 2μm. Load resistance R_L is set to 100Ω. The extinction ratio (ER, $\mathcal{R}_{ER}$) is treated as a requirement parameter. The cavity length L_g is then set to satisfy the minimum requirement of 10dB ER:

$$L_g = \ln(\mathcal{R}_{ER})/(\Gamma_c \Delta\alpha) \tag{12}$$

Two important practical properties describing the performance of the modulator can be linked to the figures of merit discussed above. The first is the ratio of maximum bandwidth to the swing voltage [45]. Assuming the maximum bandwidth is only related to the time constant $R_L C$, we have $\Delta f = 1/(2\pi R_L C) = d_i/(\epsilon_s \pi R w_g L_g)$. The voltage applied to the intrinsic region is $V_i = F d_i$. Then, using Eq.(12), we obtain the expression independent on the cavity length:

$$\frac{\Delta f}{\Delta V} = \frac{\Gamma_c}{\epsilon_s \pi R_L w_g \ln(\mathcal{R}_{ER})}\left(\frac{\Delta\alpha}{\Delta F}\right) \tag{13}$$

The second important parameter is the switching power per bit P_{ac}/N_B.[47] Combining with Eq.(12), P_{ac}/N_B is:

$$\frac{P_{ac}}{N_B} = \frac{1}{2} C \Delta V^2 = \frac{1}{2} \epsilon_s w_g L_g d_i \Delta F^2 = \frac{\ln(\mathcal{R}_{ER})\, \epsilon_s w_g d_i}{2\Gamma_c}\left(\frac{\Delta\alpha}{\Delta F^2}\right)^{-1} \tag{14}$$

It is clear from Eq.(13) and Eq.(14) that, with the same ER, increasing the figures of merit $\Delta\alpha/\Delta F$ and $\Delta\alpha/\Delta F^2$ is equivalent to increasing the bandwidth per volt and decreasing the drive power per bit.

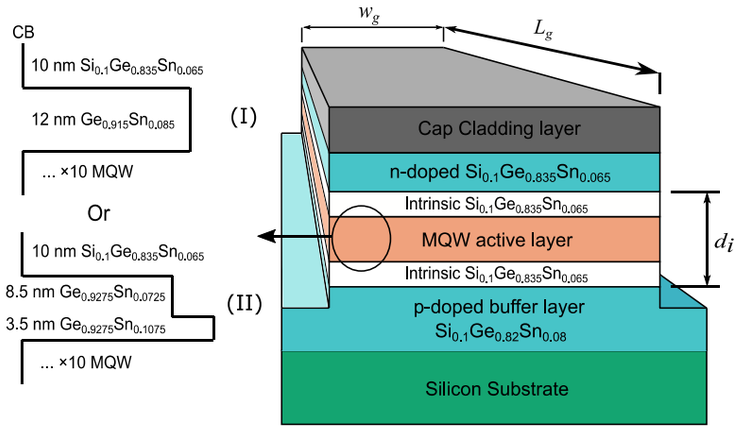

Fig.12. Schematic diagram of the waveguide design. The layer with 10 MQWs is using either square QWs (structure I) or intra-step QWs (structure II), and they have the same total thickness.

The absorption spectra and figures of merit for structure I and II are shown in Fig.13. The maximum absorption change and figures of merit at 2340nm are achieved at 65kV/cm and 50kV/cm for square QW and intra-step QW respectively. For the square QW, the absorption coefficient in the "on transmitting state" (0kV/cm) is 342cm^{-1} and in "off absorbing state" (65kV/cm) it is 1760cm^{-1}. For the intra-step QW the corresponding values are 336cm^{-1} in the on state and 1900 cm^{-1} in the off state. Therefore, the absorption change after including the optical confinement factor, $\Gamma_c \Delta\alpha$, is 510 cm^{-1} for the square QW and 563 cm^{-1} for the intra-step QW. For the square QW, we also present the result when a moderate, 15kV/cm, on-set applied field is used, the on-set voltage will then be 0.5V. The swing voltage is then reduced, to the same value as in the intra-step QW, with a fairly small increase in residual absorption. In this case both figures of merit of the square QW increase, but still remain smaller than for the intra-step QW. The comparison of some practical parameters of structure I, structure II with 0kV/cm on-set, and structure I with 15kV/cm on-set are shown in Table IV. For the intra-step QW with zero on-set voltage, the bandwidth per unit applied voltage is 44% higher than for the square QW also with zero on-set voltage, and 21% higher than if the on-set is 0.5V. The power consumption of the intra-step QW is reduced by 46% and 12% when the on-set of the square QW is 0V and 0.5V, respectively. In summary, even when restricting the on-set of the intra-step QW to be zero, it can still outperform the square QW, which makes the intra-step QW more suitable for low voltage operations.

Table IV. Practical parameters of the modulator design using structure I with 0kV/cm and 15kV/cm on-set, and structure II with only 0kV/cm on-set.

MQW Type	L_g [a] (μm)	V_i^{on} (V)	ΔV (V)	IL[b] (dB)	Maximum Bandwidth[b] (GHz)	$\Delta f/\Delta V$ [b] (GHz/V)	P_{ac}/N_B [b] (fJ/bit)
Square QW (I)	45.1	0	2.15	2.4	41.1	19.1	89
Square QW (I)	46.3	0.5	1.65	2.7	39.9	24.2	54.2
Intra-step QW (II)	40.8	0	1.65	2.1	45.3	27.5	47.8

[a]Calculated by Eq.(12) to achieve a 10dB ER.
[b]Calculated according to the cavity length and assuming the load resistance is 100Ω.

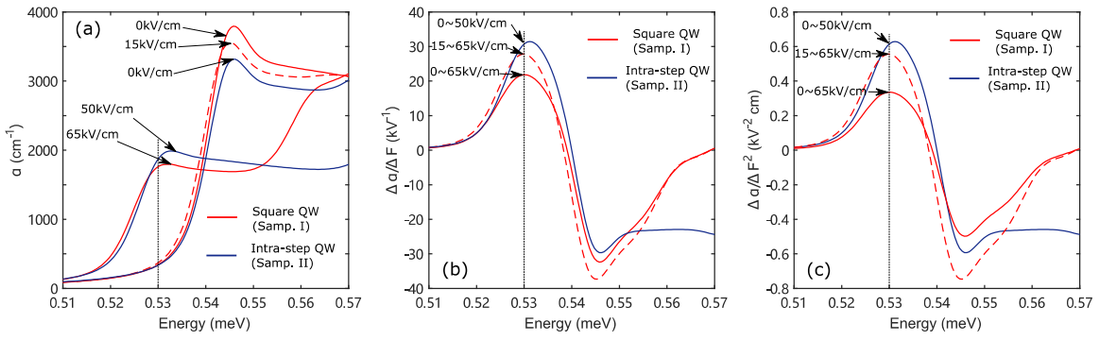

Fig.13. (a) Absorption spectra of structure I at 0kV/cm, 15kV/cm and 65kV/cm, structure II at 0kV/cm and 50kV/cm. The maximum absorption change is achieved at 65kV/cm and 50kV/cm for structures I and II, respectively. (b) Figure of merit $\Delta\alpha/\Delta F$ corresponding to (a). (c) Figure of merit $\Delta\alpha/\Delta F^2$ corresponding to (a).

IV. Conclusion

In this work we have used 8-band **k.p** theory combined with variational method to calculate the optical properties of MQWs based on Group-IV materials. The methodology provides good agreement with experimental results after some calibration of the input parameters. We have used this model to study intra-step QW structures. The alloy compositions of such structures were limited so that their transition energies lay in the MIR spectral region (wavelength larger than ~2μm). By analysing the QCSE using perturbation method, we found that the Stark shift of the intra-step QW is not always larger than that of a square QW with the same size. The Stark shift behavior of the intra-step QW can be engineered by control of the potential profile. A much larger Stark shift is observed when the structure is designed so that the first heavy-hole state is at the top of the deeper intra-well (i.e. at the band edge of the shallower intra-layer). We expect that the largest Stark shift could be achieved by using extremely narrow and deep intra-well. However, the improvement obtained from this extreme case is limited by the total well width and this, together with difficulties in growing such structures, makes it hard to recommend it for real applications. Then we also compared the square QW and intra-step QW using two different figures of merit: $\Delta\alpha/\Delta F$ and $\Delta\alpha/\Delta F^2$. These two figures of merit are directly related to the bandwidth per volt and power consumption per bit when considering a waveguide design with the same extinction ratio. The intra-step QW shows a significant advantage over a square QW when they both use zero on-set voltage, and the intra-step QW with zero on-set is still better in all aspects compared to the square QW with a 15kV/cm (0.5V) on-set. Using a high applied field region for modulation can help to reduce the swing voltage and this may make the figure of merit of square QW higher than for the intra-step QW using zero on-set. But the trend for EPIC primarily targets the low voltage operation, and an intra-step QW is then obviously a more suitable choice for EA modulators. This work only analyzed the performance of a simple asymmetric QW structure, but in general it is possible to design more complicated broken-symmetry structures to further improve the performance, albeit at the expense of greater complexity of epitaxial growth.

Appendix: The polynomial expresion of the function G(x)

The function $G(x)$ is defined as an integral:

$$G(x) = \int_0^\infty dt \frac{e^{-xt}}{(1+t^2)^{3/2}} \tag{15}$$

In order to reduce the calculation time, the function $G(x)$ in Eq.(3) is using the polynomial expression from [25]. The maximum error of this expression is less than 1.5%.

$$G(x) = \begin{cases} 1 - 0.89707x - 0.25262x^2 \ln\left(\frac{x}{2}\right) + 0.22576x^2 \\ +3.2373 \times 10^{-2}x^3 - 4.1369 \times 10^{-2}x^4 \ln\left(\frac{x}{2}\right), \quad (0 < x \le 6.8) \\ \frac{1}{x} - \frac{3}{x^3} + \frac{45}{x^5} - \frac{1575}{x^7}, \quad (x > 6.8) \end{cases} \tag{16}$$

Note that $G(x)$ is a symmetric function, hence $G(x) = G(-x)$, and $G(0) = 1$.

PLEASE CITE THIS ARTICLE AS DOI: 10.1063/5.0067803

Data Availability Statement

The data that support the findings of this study are available from the corresponding author upon reasonable request.

References

[1] S. Wirths et al., Nat. Photonics 9, 88 (2015)
[2] Q. M. Thai et al., Opt. Express 26, 32500 (2018).
[3] Y. Zhou et al., Optica 7(8), 924–928 (2020).
[4] J. Margetis et al., Appl. Phys. Lett. 113, 221104 (2018).
[5] G. Chang and C. Chang, 7th IEEE International Conference on Group IV Photonics, pp 87-89 (2010)
[6] G. Chang and C. Chang, IEEE J. Quantum Electron. 48, pp. 533-541. (2012)
[7] L. Lever, et al., Journal of Lightwave Technology 28, pp. 3273-3281 (2010)
[8] J. Gao, et al., AIP Advance 7, 035317 (2017)
[9] Y. Kuo, et al., Nature 437, 1334-1336 (2005)
[10] Rebecca K. Schaevitz, et al., IEEE Journal of Selected Topics in Quantum Electronics 14, pp. 1082-1089 (2008)
[11] J. E. Roth, et al., Opt. Express 15, pp. 5851-5859 (2007)
[12] N. Yahyaoui, et al., Superlattices and Microstructures 85, pp. 629-637 (2015)
[13] R. Ponce, et al., 2017 IEEE 14th International Conference on Group IV Photonics, pp. 19-20 (2017)
[14] M. Akie, et al., IEEE Journal of Selected Topics in Quantum Electronics 24, pp. 1-8 (2018)
[15] Y. Hsieh, et al., Commun. Mater. 2, 40 (2021)
[16] P. Chaisakul, et al., Opt. Express 20, 3219 (2012)
[17] T. Fujisawa, et al., IEEE J. Quantum Electron. 51, pp. 1-7 (2015)
[18] M. Morita, et al., Jpn. J. Appl. Phys. 29, L1663 (1990)
[19] T. Tütken, et al., Appl. Phys. Lett. 63, 1086 (1993)
[20] D. Shin et al., J. Appl. Phys. 89 1515 (2001)
[21] Abedi, K, The European Physical Journal – Applied Physics 56, 10403 (2011)
[22] T. K. Woodward, et al., J. Appl. Phys. 78, 1441 (1995)
[23] D. J. Paul, Phys. Rev. B 77, 155323 (2008)
[24] Z. Chen, et al., J. Appl. Phys. 129, 123102 (2021)
[25] P. J. Mares and S. L. Chuang, J. Appl. Phys. 74, 1388 (1993)
[26] S. L. Chuang, Phys. Rew. B 43, 1500 (1991)
[27] S. L. Chuang *Physics of Photonic Devices - 2nd Edition*, (John Wiley & Sons, 2012)
[28] Y. Huang, et al., J. Appl. Phys. 77, pp. 11-16 (1995)
[29] S. A. Claussen, et al., Optics Express 18, pp. 25596-25607 (2010)
[30] A. B. McLean, et al., J. Electron. Spectr. Related Phenom. 69, pp. 125-132, (1994)
[31] R. K. Schaevitz, et al., AIP. Advances 1, 032164 (2011)
[32] G. G. Macfarlane and V. Roberts, Phys. Rev. 97, 1714 (1955)
[33] D. Rainko, et al., Sci. Rep. 8, 15557 (2018)
[34] D. J. Paul, J. Appl. Phys. 120, 043103 (2016)
[35] M. P. Polak, et al., J. Phys. D: Appl. Phys. 50, 195103 (2017)
[36] G. Chang, et al., IEEE J. Quantum Electron. 46, pp. 1813-1820 (2010)
[37] S. Adachi, *Properties of Group IV, III-V and II-VI Semiconductors* (Wiley, New York, 2009)
[38] H. H. Li, J. Phys. Chem. Ref. Data 9, 561 (1993)
[39] A. I. Golovashkin and G. P. Motulevich, Sov. Phys. JETP 19, 310 (1964)
[40] J. A. Van Vechten, Phys. Rev. 182, 891 (1969)
[41] P. Moontragoon et al., Semicond. Sci. Technol. 22, 742 (2007)
[42] J. D. Gallagher et al., Appl. Phys. Lett. 103, 202104 (2013)
[43] S. Q. Liu and S. T. Yen, J. Appl. Phys. 125, 245701 (2019)
[44] J. Liu, et al., Phys. Rev. B 70, 155309 (2004)
[45] M. K. Chin, IEEE Photonics Technology Letters 4, pp. 726-728 (1992)
[46] E. Bigan, et al., Electronics Letters 26, pp. 355-357 (1990)
[47] M. K. Chin, et al., IEEE J. Quantum Electron 29, pp. 2476-2488 (1993)
[48] J. Thalken, et al., Appl. Phys. Lett. 85, 121 (2004)
[49] H. Takeuchi, et al., IEEE Journal of Selected Topics in Quantum Electronics 3, pp. 336-343 (1997)

PLEASE CITE THIS ARTICLE AS DOI: 10.1063/5.0067803

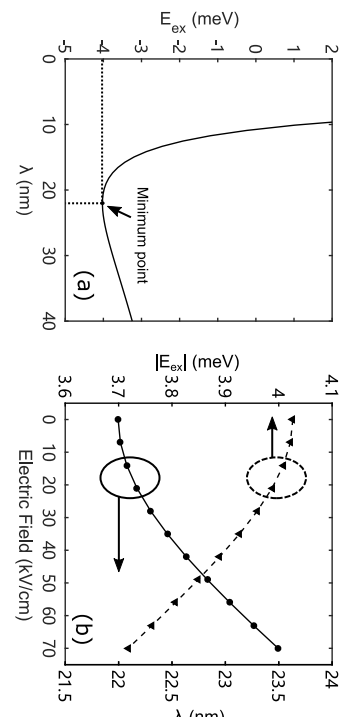

AIP Publishing

Journal of Applied Physics

ACCEPTED MANUSCRIPT

PLEASE CITE THIS ARTICLE AS DOI: 10.1063/5.0067803

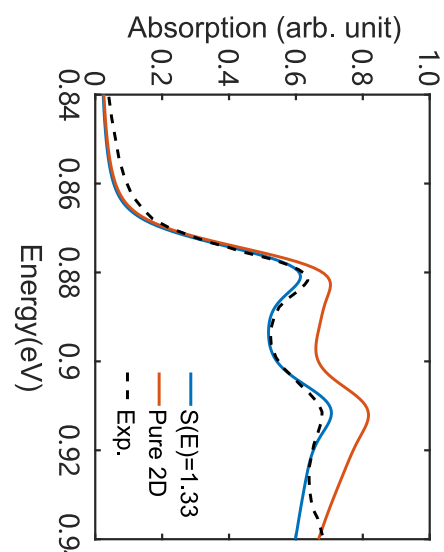

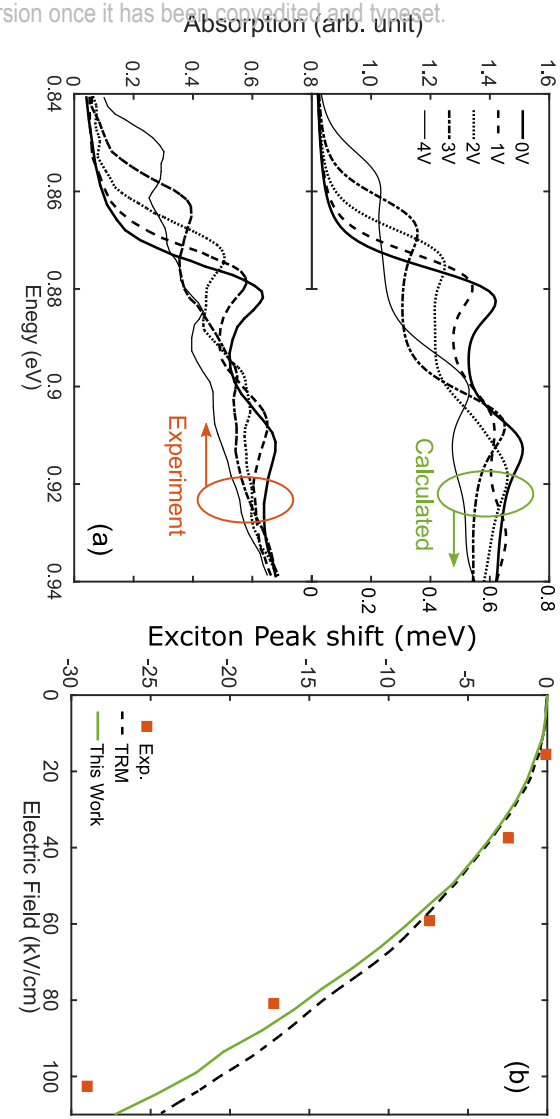

AIP Publishing

Journal of Applied Physics

ACCEPTED MANUSCRIPT

PLEASE CITE THIS ARTICLE AS DOI: 10.1063/5.0067803

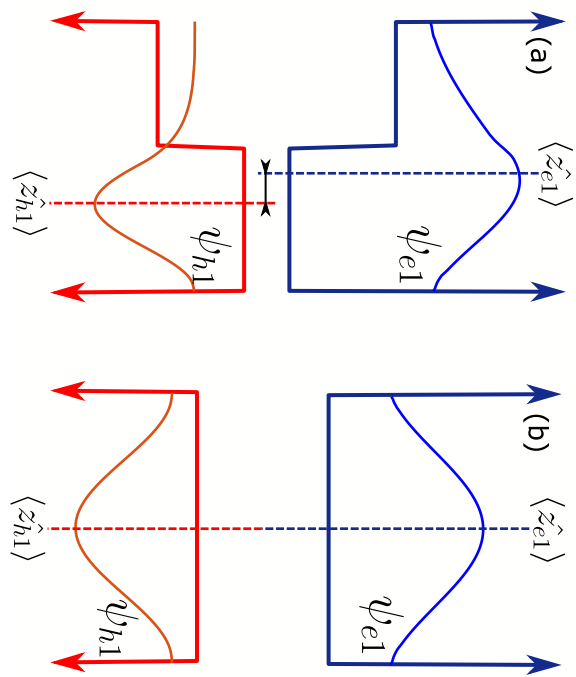

AIP Publishing

Journal of Applied Physics

ACCEPTED MANUSCRIPT

PLEASE CITE THIS ARTICLE AS DOI: 10.1063/5.0067803

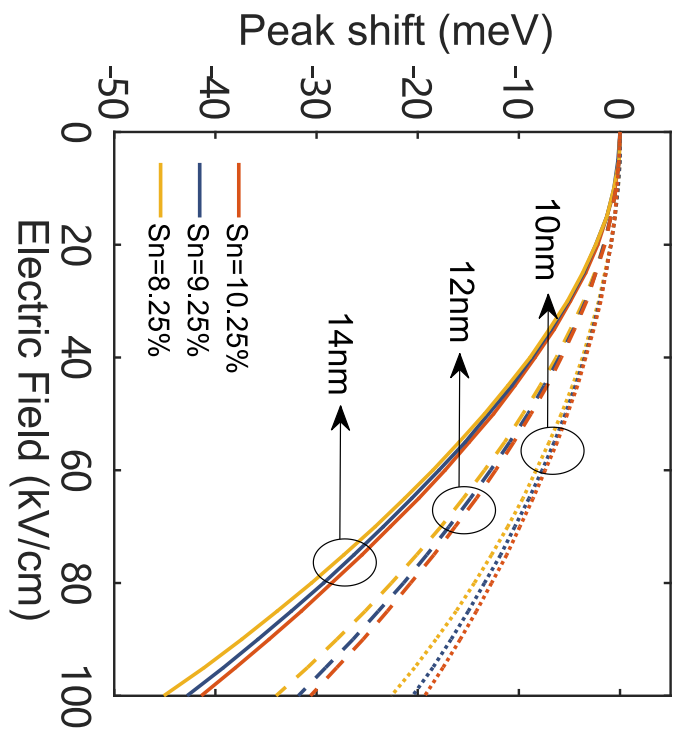

AIP Publishing

Journal of Applied Physics

ACCEPTED MANUSCRIPT

PLEASE CITE THIS ARTICLE AS DOI: 10.1063/5.0067803

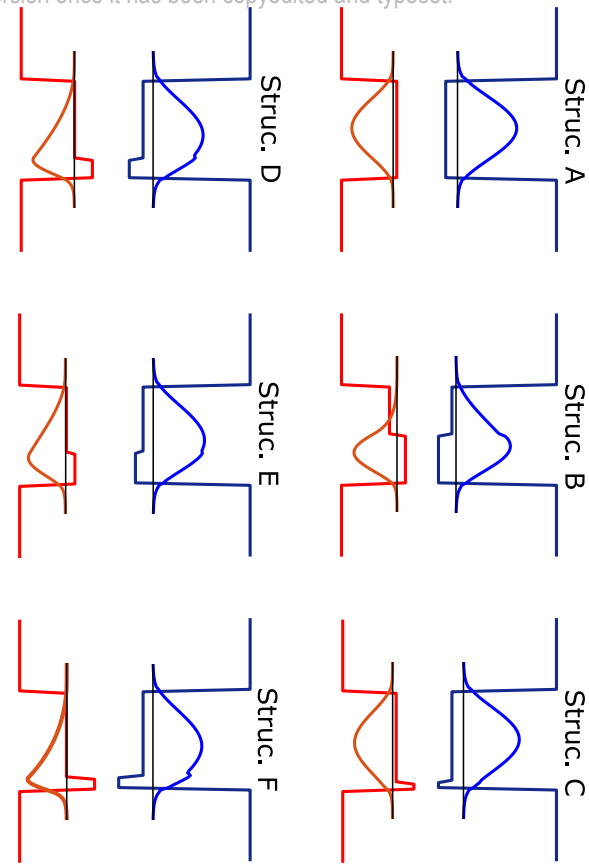

AIP Publishing

Journal of Applied Physics

ACCEPTED MANUSCRIPT

PLEASE CITE THIS ARTICLE AS DOI: 10.1063/5.0067803

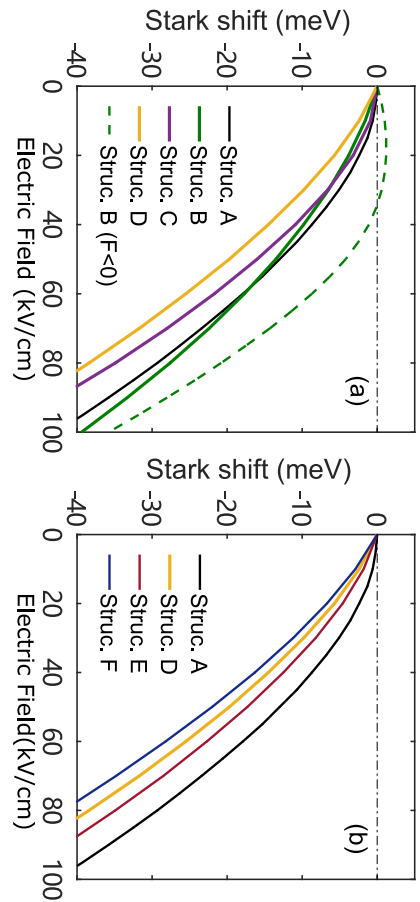

AIP Publishing

Journal of Applied Physics

ACCEPTED MANUSCRIPT

PLEASE CITE THIS ARTICLE AS DOI: 10.1063/5.0067803

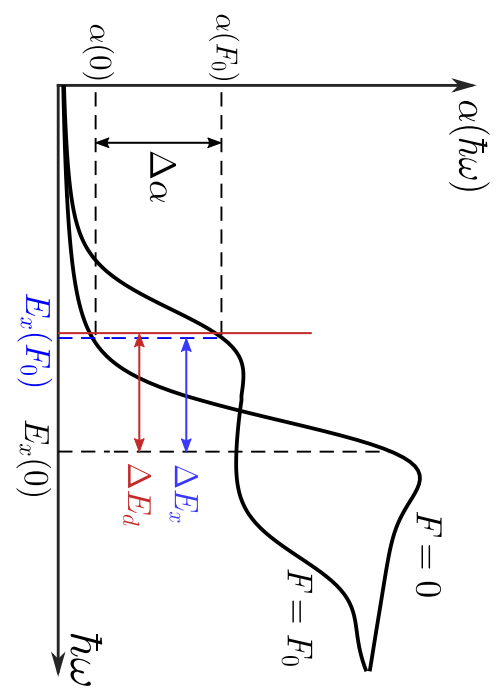

Journal of Applied Physics

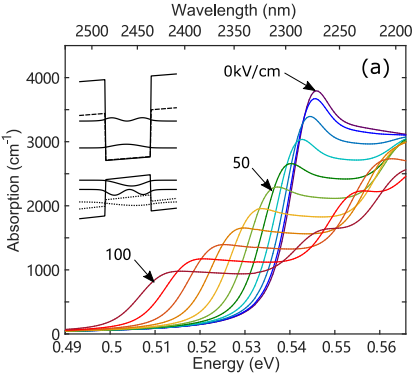

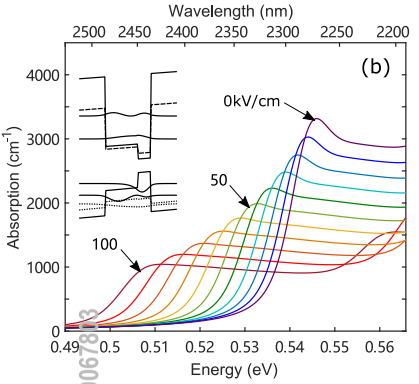

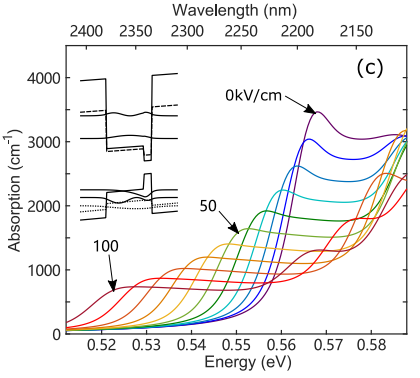

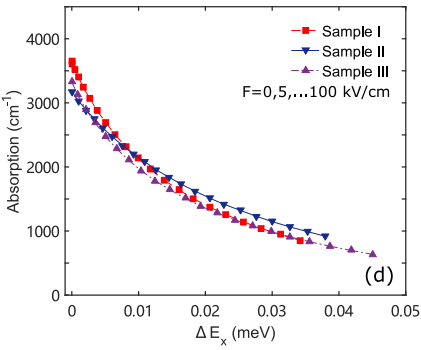

AIP Publishing

Journal of Applied Physics

PLEASE CITE THIS ARTICLE AS DOI: 10.1063/5.0067803

PLEASE CITE THIS ARTICLE AS DOI: 10.1063/5.0067803

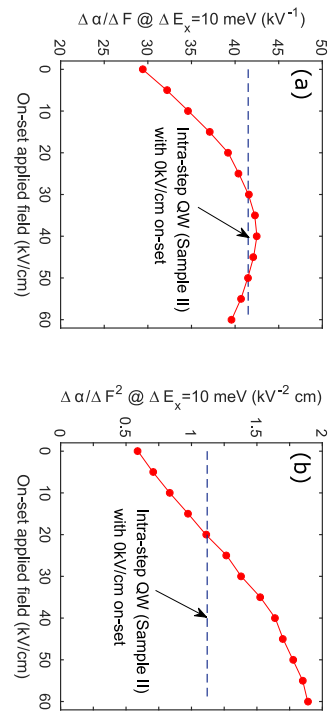

AIP Publishing

Journal of Applied Physics

PLEASE CITE THIS ARTICLE AS DOI: 10.1063/5.0067803

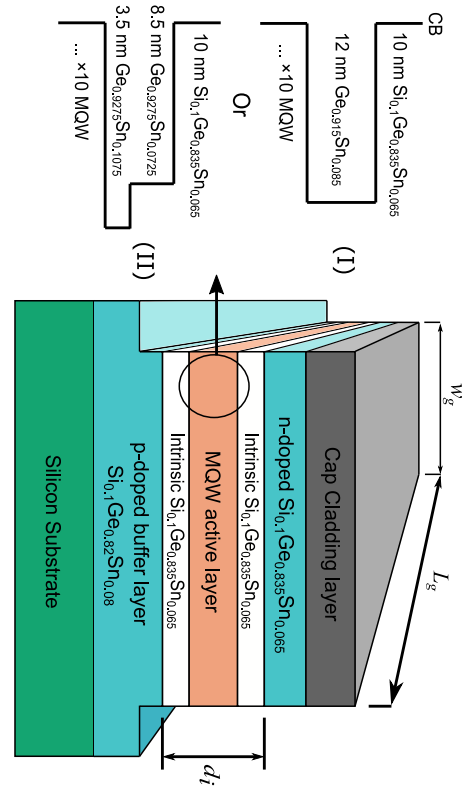

AIP Publishing

Journal of Applied Physics

PLEASE CITE THIS ARTICLE AS DOI: 10.1063/5.0067803